DTU Library

3D microstructural characterization of Ni/yttria-stabilized zirconia electrodes during long-term CO_2 electrolysis

Shang, Yijing; Smitshuysen, Anne Lyck; Yu, Miao; Liu, Yuliang; Tong, Xiaofeng; Jørgensen, Peter Stanley; Rorato, Léa; Laurencin, Jerome; Chen, Ming

Published in:
Journal of Materials Chemistry A

Link to article, DOI:
10.1039/d3ta01503c

Publication date:
2023

Document Version
Peer reviewed version

3D microstructural characterization of Ni/yttria stabilized zirconia electrodes in long-term CO_2 electrolysis

Received 00th January 20xx,
Accepted 00th January 20xx

DOI: 10.1039/x0xx00000x

Yijing Shang,[a] Anne Lyck Smitshuysen,[a,b] Miao Yu,[a] Yuliang Liu,[a,c] Xiaofeng Tong, [d] Peter Stanley Jørgensen,[a] Léa Rorato,[e] Jérôme Laurencin,[e] Ming Chen [a,*]

The solid oxide electrolysis cell (SOEC) is one of the most promising energy conversion devices due to its high efficiency and gas flexibility. However, its performance degradation in long-term operation limits its commercialization. Among different phenomena, the degradation of the Ni/yttria stabilized zirconia (YSZ) fuel electrode during long-term operation is recognized as one of the main causes for the loss in cell performance. A lot of work have been already devoted to investigating the degradation of Ni/YSZ electrodes in steam electrolysis, whereas only limited studies look into the Ni/YSZ electrode stability after long-term CO_2 electrolysis. In this work, the microstructure evolution of Ni/YSZ electrodes after long-term operation in CO/CO_2 atmosphere is investigated. For this purpose, the Ni/YSZ supported planar type SOEC cells are operated at 800 °C and -1 A/cm^2 or zero current, with a mixture of CO_2/CO (90/10) supplied to the Ni/YSZ electrode. The 3D electrode microstructures for the pristine cermet (reference) and after 1000 h operation are reconstructed. Significant loss of Ni in the active electrode is observed in the cell operated at -1 A/cm^2 for 1000 h, along with an increased Ni fraction in the support layer. An increase of the Ni particle size (i.e. Ni coarsening) is also observed. In the cell operated with zero current for 1000 h, only Ni coarsening but no Ni migration is observed. Our results show that Ni migration away from the electrode/electrolyte interface happens also during long-term CO_2 electrolysis, to a similar extent as in steam electrolysis.

Introduction

With the increasing energy demand, the rapid consumption of fossil fuels and the accompanying environmental problems are progressively pushing the transition toward renewable and clean energy scenarios [1]. However, significant issues related to energy conversion and storage need to be addressed due to the intermittency of renewable energy sources such as solar or wind energy. The solid oxide electrolysis cell (SOEC) is considered nowadays as one of the most promising energy conversion devices, which can convert renewable electricity to chemicals and fuels that can be more easily stored and transported. However, its performance degradation in long-term operation limits its commercialization. It has been found that degradation of the Ni/yttria stabilized zirconia (YSZ) fuel electrode in SOECs during long-term operation is one of the prime causes accounting for the loss in cell performance [2, 3].

A lot of studies have been devoted to investigating the degradation of Ni/YSZ electrodes after long-term steam electrolysis. By comparing the degradation of two SOEC cells in long-term steam electrolysis, The et al. [4] proposed that the Ni depletion at the electrode/electrolyte interface and the Ni agglomeration at the inner part of the Ni/YSZ electrode are the main causes of cell performance loss. Fang et al. [5] utilized scanning electron microscopy (SEM) in combination with the impedance measurement and DRT analysis on a SOEC cell tested for 20000 h. They found that the main degradation comes from the continuously increased ohmic resistance, which is mainly attributed to a decrease in the effective conductivity of the fuel electrode because of Ni depletion in the active layer. Hoerlein et al. [6] systematically studied the influence of operating parameters, such as temperature, fuel gas humidity, and current density, on the individual degradation processes through a series of long-term degradation measurements of SOEC cells. They proposed that the mechanism of Ni transport for the Ni migration could be explained by the formation of volatile $Ni(OH)_x$ species [7]. Trini et. al. [8] investigated the degradation of Ni/YSZ cermet exposed to a mixture of H_2O/H_2 (50/50) and tested at 800 °C for 1000 h in both fuel cell and electrolysis modes. They found that Ni coarsening occurs in both SOFC and SOEC modes, whereas Ni depletion can only be observed at the electrode/electrolyte interface in SOEC mode. This microstructural evolution was considered as the main reason explaining the SOEC performance degradation. Moussaoui et al. built a model to predict the Ni agglomeration during long-term operation in SOEC mode by using a mathematical morphology approach [9]. Sun et al. [10] analyzed the porosity change and Ni redistribution using SEM images of SOEC cells tested in $H_2O + CO_2$ co-electrolysis for 1000 h.

A number of research groups have looked into the degradation mechanisms of Ni/YSZ electrodes in SOEC [4, 5, 8, 11-17]. The microstructural degradation of Ni/YSZ includes Ni particle coarsening in the bulk and migration over long distances (i.e. Ni redistribution). Two mechanisms have been proposed to account for Ni evolution in the cermet: 1) A classical Ostwald ripening process for which, Ni atoms are emitted from one Ni particle, migrate over the YSZ or in the vapor phase, and get captured by another Ni particle, and 2) Ni particle migration over the YSZ phase followed by coalescence with other Ni clusters (particle migration and coalescence, PMC). For both cases, in case of no other driving forces then, the transport of Ni will be driven by the difference in Ni surface energy between small and large particles. Several different mechanisms have been proposed [18] to explain the Ni migration over long distance in the cermet. It has been found by Hauch et al. that in SOEC

a. Department of Energy Conversion and Storage, Technical University of Denmark, 2800, Kgs. Lyngby, Denmark
b. DynElectro ApS, 4130, Viby Sjaelland, Denmark
c. School of Materials Science and Engineering, Henan University of Science &Technology, 471023, Luoyang, China
d. Institute of Energy Power Innovation, North China Electric Power University, 102206, Beijing, China.
e. Univ. Grenoble Alpes - CEA/LITEN, 38054, Grenoble, France

mode, Ni migrates towards electrolyte at high current density and temperatures above 950 °C [11], and they explained this as Ni migrates down the gradient of the pH_2O/pH_2 ratio in the form of $Ni(OH)_x$ gas species. Whereas at lower temperatures and under high polarization, a pronounced Ni migration away from the electrolyte is observed [7, 12]. In this case, the mechanism based on Ni migration with $Ni(OH)_x$ volatile molecules in the gas phase seems unlikely [16, 18]. On the other hand, Jiao et al. found that the variation of the interface free energy between Ni and YSZ could account for the Ni migration in steam electrolysis [19, 20]. Due to the contradictions among experimental findings from different research groups, the mechanism of Ni migration still needs to be investigated. Moreover, most of the published articles focused on the microstructure evolution of active fuel electrodes in steam electrolysis, whereas, to the best of our knowledge, no studies have been devoted to characterizing the potential Ni migration at the electrode/electrolyte interface after long-term CO_2 electrolysis. The degradation of the Ni-YSZ electrode in CO_2 electrolysis differs from the one in steam electrolysis, not only with regard to electrochemistry, but also in the aspect that potential carbon deposition may happen in CO_2 electrolysis. These have been discussed in detail in literature [21-23]. With regard to Ni migration, the degradation behavior is rather similar as we will report in the current work. The observed difference may be caused by two factors: 1) the different reaction kinetics between CO_2 reduction and steam splitting, thus resulting in different over-potential of the Ni-YSZ electrode and hence different driving forces for Ni migration; 2) the pathway and kinetics of Ni diffusion in CO_2 and steam and its impact on Ni migration, which remains unclear for the moment.

In this work, the microstructure evolution of the Ni/YSZ electrodes after long-term operation in the CO/CO_2 atmosphere is investigated. Ni/YSZ-supported planar-type SOEC cells are operated with a mixture of CO_2/CO (90/10) at 800 °C and -1 A/cm^2 or zero current. Electrode microstructures are reconstructed at the cell inlet by focused ion beam - scanning electron microscopy (FIB-SEM) tomography for a pristine cermet in its reduced state (reference) and after around 1000 h operation with different constant current densities (0 and -1 A/cm^2). By analyzing and comparing the 3D microstructure parameters of the three cells, the Ni/YSZ degradation in CO_2 electrolysis is investigated. In addition, the effect of Ni redistribution on the support layer of the Ni/YSZ electrode is studied as well. The mechanism of Ni/YSZ electrode degradation in CO_2 electrolysis is discussed by comparing the quantitative microstructure analysis in this work with the one for steam electrolysis published previously. Based on the obtained results, the driving force of the observed Ni migration in CO_2 electrolysis is discussed. The detailed electrochemical performance analysis of the SOEC CO_2 electrolysis will be reported elsewhere.

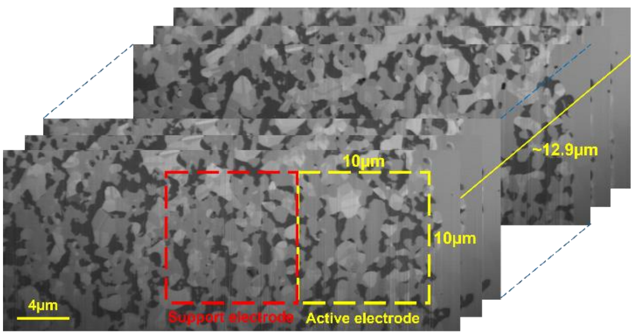

Fig. 1 FIB-SEM cross-sections obtained from the SE2 detector along the milling front direction. (YSZ is dark gray, Ni is light gray, and the pore phase is black.)

Experiments

The cells used in this study are planar fuel electrode-supported solid oxide cells, which consist of a Ni/3YSZ (3 mol% Y_2O_3 stabilized ZrO_2) support layer (~300 µm in thickness), a Ni/8YSZ active fuel electrode (10~15 µm), an 8YSZ electrolyte (~8 µm), a CGO ($Ce_{0.9}Gd_{0.1}O_{1.95}$) barrier layer (~5 µm), and an LSCF/CGO (LSCF: $La_{0.6}Sr_{0.4}Co_{0.2}Fe_{0.8}O_{3-\delta}$) oxygen electrode (~25 µm). These cells have a footprint of 5.3×5.3 cm^2, with an active area of 4×4 cm^2 where an LSM ($La_{1-x}Sr_xMnO_3$) contact layer was screen-printed on top of the oxygen electrode.

The cells were tested in an alumina cell test house, and further details about the experimental procedure can be found elsewhere [17]. To reduce the NiO in the fuel electrode to Ni, the cells were exposed to dry safety hydrogen (N_2/H_2 = 95/5) at 850 °C for 2 h and hereafter to humid hydrogen (H_2O/H_2 = 4/96) for 2 h. Then, one of the reduced cells was taken out and cooled down to room temperature, as the reference cell for microstructure analysis (hereafter called Cell_Ref in this work). The other two cells were exposed to performance characterization and a durability test for more than 1000 h at constant current density (0 or -1 A/cm^2) under CO_2 electrolysis. According to the current density of the durability test condition, the cells are named Cell_0A and Cell_1A, respectively. The performance characterization was carried out with *iV* and AC electrochemical impedance spectra (EIS) measurements. The durability tests were operated under galvanostatic conditions at 800 °C with 13.4 L/h CO_2/CO (90/10) supplied to the Ni/YSZ electrode and 50 L/h O_2 to the LSCF/CGO electrode. The reactant conversion for Cell_1A was 56%. EIS was measured using a Solartron 1255 frequency analyzer and an external shunt resistor connected in series with the cell. The spectra data were recorded within a range from 96850 Hz to 0.08 Hz with 12 points per frequency decade. Analyses of the impedance data and *iV* curves were performed using the in-house developed software RAVDAV [24].

The microstructural characterization was performed at a location taken at the cell inlet to ensure that all the analyzed samples were exposed to the same gas composition as the gas supply. The three cell pieces were embedded into epoxy resin and polished for the SEM analysis and FIB-SEM tomography. The SEM images were obtained with the Zeiss Merlin SEM. The accelerating voltage is 15 kV for EsB images, and 0.95 kV for low voltage images. The EsB images can be used to analyze the porosity of samples. However, the contrast between Ni and YSZ phases in these images is low. The low voltage images recorded with the Inlens detector allow detecting the percolating Ni network which appears much brighter than the other phases.

3D image sets were collected using FIB serial sectioning with a Zeiss XB1540 Crossbeam microscope on the Cell_Ref and the inlet side of interest in the tested cells (Cell_0A and Cell_1A). Two sets of images obtained from Inlens and SE2 detectors were recorded for each sample and used for post-processing and segmentation. More details on the FIB-SEM serial sectioning and the image post-processing can be found in Ref [25]. Fig. 1 shows a series of raw images obtained from the SE2 detector during FIB-SEM serial sectioning, and the milling front direction is presented in the picture. The 3D reconstructions were performed on the representative area highlighted by the yellow (as the active electrode) and red (as the support layer) rectangles in Fig. 1. Although the cells were made in the same batch and the thickness of the active fuel electrode was expected to be about 10 µm, the actual thickness of the active electrode is 12-14 µm (as shown in Fig. 3). The structural inhomogeneity of the area near the interfaces of electrolyte/active electrode and active electrode/support layer can cause some unexpected errors in 3D data analysis. In this work, the location for the electrode/electrolyte interface is defined as where the YSZ phase fraction drops down from 100% and becomes relatively stable (further illustrated in Figs. 1&6). 10 µm from the electrode/electrolyte interface into the electrode is then chosen as the active electrode for all three cells. The 10 µm thick region next to the active electrode belongs to the support layer (it might contain around 2-3 µm active electrode microstructure, but we still call it support layer in this work). Different voxel sizes and dimensions of the sub-volumes were used for the three samples due to slightly different microscope setups used in the study. The overall 3D reconstruction volume is ~$10 \times 22 \times 12.9$ µm^3. To have the same analyzed volume for the three samples, the maximum size of the sub-volume extracted from the data sets was ~ $10 \times 10 \times 12.9$ µm^3, i.e. for each sample a volume of $10 \times 10 \times 12.9$ µm^3 active electrode plus a volume of $10 \times 10 \times 12.9$ µm^3 neighboring support layer. The detailed voxel sizes are $25 \times 25 \times 35.92$ nm^3, $25 \times 25 \times 34.14$ nm^3, and $25 \times 25 \times 40.74$ nm^3 corresponding to the sub-volume size of $400 \times 400 \times 359$ pixels, $400 \times 400 \times 378$ pixels, and $400 \times 400 \times 317$ pixels for the active electrode and support layers of Cell_Ref, Cell_0A and Cell_1A, respectively. Microstructural parameters, including continuous particle size distribution (PSD) [26], phase volume fractions, total and percolating triple phase boundaries (TPBs) [27], and percolating sites versus critical pathway diameter [25], were computed on the segmented volumes. The properties obtained after long-term operation at 0 or -1 A/cm^2 in CO_2 electrolysis were compared to the ones calculated for the reference (Cell_Ref).

Results

Fig. 2 presents the electrochemical performance of Cell_0A and Cell_1A before and after the long-term test and evolution of the cell voltages during the durability testing period. As expected, the two cells behaved differently when exposed to different current densities. As shown in Fig. 2a, Cell_0A has an initial voltage of 881.73 mV, which remained constant over the entire period. The cell voltage of Cell_1A started at 1199.73 mV, increasing steadily with an average degradation rate of 8.2 %/kh. Fig. 2b compares the *iV* curves of the two cells measured before and after the durability tests. They were measured at 800 °C with 24 L/h H_2/H_2O (50/50) supplied to the fuel electrode and 50 L/h O_2 to the oxygen electrode. The two cells showed similar performance before the durability test and different degrees of performance degradation after. As expected, larger degradation can be seen in the cell exposed to the current, i.e., Cell_1A, as reflected in the slope of the *iV* curves. The measured OCVs for Cell_0A are 969.1 and 968.8 mV, and for Cell_1A are 972.2 and 972.8 mV, before and after the durability test, respectively, all quite close to the calculated theoretical Nernst potential (977.1 mV), showing gas tightness of the cells and the test setup. Fig. 2c presents the Nyquist plots of the EIS data recorded before and after the durability tests under the same conditions as for the *iV* measurements. For Cell_0A, the serial resistance R_s remained unchanged whereas the polarization resistance R_p increased slightly after the durability test. On the contrary, both R_s and R_p increased significantly for Cell_1A after being operated at -1 A/cm^2 for 1083 hours. This variation confirms that a more pronounced cell degradation occurred when the cell was operated at a high current load of -1 A/cm^2, as indicated in the *iV* curves. It is speculated that the increase in R_s value may be attributed to the migration of Ni away from the fuel electrode/electrolyte interface during the electrolysis operation, resulting in a significant Ni depletion in the active area. This results in an increase of the effective thickness of the YSZ layer responsible for the transportation of oxygen ions [7]. The distribution of relaxation times method (DRT) was used to further analyze the different contributions to the overall R_p. In DRT plots (Fig. 2d), each peak represents an electrochemical process, and the integral area underneath represents the corresponding resistance of that specific electrochemical process [28-30]. In our previous studies carried out on the same type of cells [8, 17, 31-34], we have found that the peaks centred at ~20 kHz, ~10 kHz, ~0.5 kHz were characterized by a pronounced thermal activation while the peaks centred at ~50 Hz and 1-10 Hz were not temperature sensitive. This strongly suggested that the peaks centred at ~20 kHz, ~10 kHz, ~0.5 kHz corresponded to the chemical and electrochemical processes in the electrodes and the peaks centred at ~50 Hz and 1-10 Hz were related to gas diffusion and conversion. Furthermore, the peak centred at ~20 kHz was almost independent of the gas conditions; the peak centred at ~10 kHz was sensitive to the gas change at the fuel electrode while almost independent of the gas change at the oxygen electrode; the peak centred at ~0.5 kHz was dependent on the gas change at the oxygen electrode while almost independent of the gas change at the fuel electrode; the peaks centred at ~50 Hz and 1-10 Hz were dependent on the gas change at both electrodes. Therefore, the peak centered at ~20 kHz is related to the transport of the O^{2-} ions through the ionic conducting network, and this part of contribution mainly comes from the Ni/YSZ electrode; the peak centered at ~10 kHz represents the electrochemical reactions at the TPBs in the Ni/YSZ electrode; the peak centered at ~0.5 kHz is associated with the electrochemical reactions at the active sites in the LSCF/CGO electrode; and the peaks centered at ~50 Hz and 1-10 Hz are associated with the gas diffusion and gas conversion processes, respectively. The peaks observed with frequencies < 1 Hz are deemed as measurement artifacts. As shown in Fig. 2d, the most significant change was observed in the high-frequency range (>2 kHz). The integral areas under the peaks centered at 10-20 kHz increased significantly, and the peak(s) shifted towards lower frequency after the durability tests. This indicates that the main degradation during the CO_2 electrolysis comes from the Ni/YSZ electrode, corresponding to the two processes of ionic conduction and TPB reactions in the Ni/YSZ electrode. The change in Cell_1A is more significant than in Cell_0A, indicating a larger degradation of the Ni/YSZ electrode in Cell_1A. Some small changes also happen in the frequency ranges corresponding to the electrochemical process at the LSCF/CGO electrode and the gas diffusion and conversion processes. An interesting phenomenon is that the peaks corresponding to the gas diffusion and conversion shift towards higher frequency, indicating faster reaction rates.

SEM micrographs are shown in Fig. 3. Qualitative variation in porosity can be observed in EsB images (Fig. 3 a-c), and low

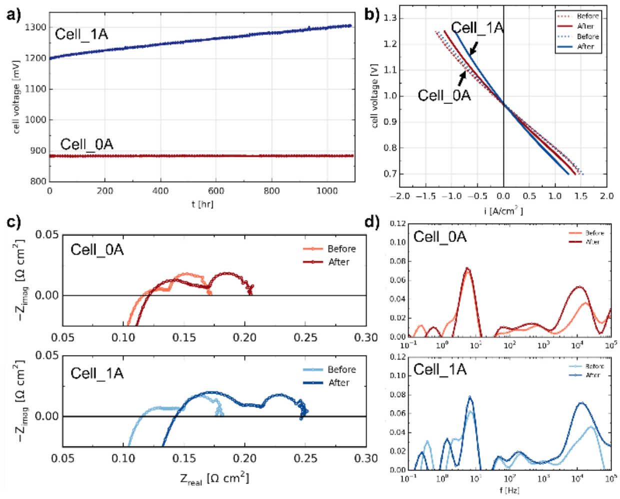

Fig. 2 Comparison of the electrochemical performance of the two cells operated at 0 A/cm² (Cell_0A) or -1 A/cm² (Cell_1A). a) Cell voltage change with time during the CO_2 electrolysis durability testing period. b) *iV* curves, c) Nyquist plots of the EIS data, and d) the corresponding DRT plots recorded before and after the durability testing period. The durability tests were performed at 800 °C with 13.4 L/h CO_2/CO (90/10) to the Ni/YSZ electrode and 50 L/h O_2 to the LSCF/CGO oxygen electrode.

voltage images obtained with the Inlens detector qualitatively illustrate the Ni percolation (Fig. 3 d-f). In Fig. 3 a-c, pores are black, and nickel and YSZ are gray, whereas in Fig. 3 d-f, the white phase is the percolating Ni, non-percolating Ni and YSZ are gray, and the pore phase is black. The SEM micrographs in Fig. 3 display the Ni/YSZ electrode degradation after the long-term aging process. By comparing the Ni/YSZ electrode microstructure of Cell_0A and Cell_1A (Fig. 3b and c) with that of Cell_Ref (Fig. 3a), it is clear that the Ni particles grow significantly after ~1000 h operation at 800 °C, both at 0 and -1 A/cm² and both in the active electrode and the support layer. From Fig. 3 d-f, it can be observed that the Ni networks of Cell_0A and Cell_1A tend to coalesce and become bigger clusters compared to Cell_Ref. Besides, Cell_1A also shows an

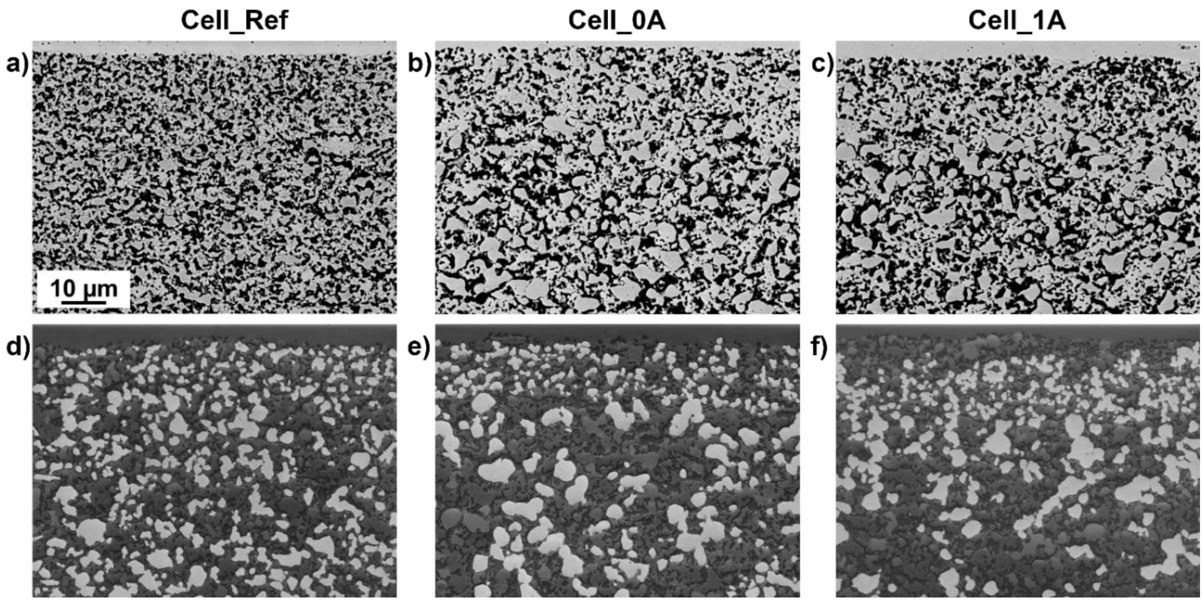

Fig. 3 EsB images of the Ni/YSZ electrode for (a) Cell_Ref, (b) Cell_0A, and (c) Cell_1A, and the low voltage images of (d) Cell_Ref, (e) Cell_0A, and (f) Cell_1A. In the EsB images pore is black, YSZ and Ni are gray. In the low voltage images recorded with the Inlens detector pores are black, YSZ and non-percolating Ni are gray, and the percolating Ni is white.

increase in pore volume fraction in the region close to the electrode/electrolyte interface though the contrast and brightness setting can affect the porosity analysis.

The 3D volumes (around 10 × 22 × 12.9 μm³) extracted from the investigated geometries for the three cells are shown in Fig. 4. The three phases of interest are represented as follows: Ni particles are red, YSZ is gray, and pores are transparent. Just by simple observation of the 3D microstructures of active electrodes, a more pronounced morphology change of the Ni phase can be found in Cell_1A compared to Cell_0A and Cell_Ref, especially at the electrolyte/electrode interface. Besides, coarser Ni particles can be observed in both Cell_0A and Cell_1A compared with Cell_Ref.

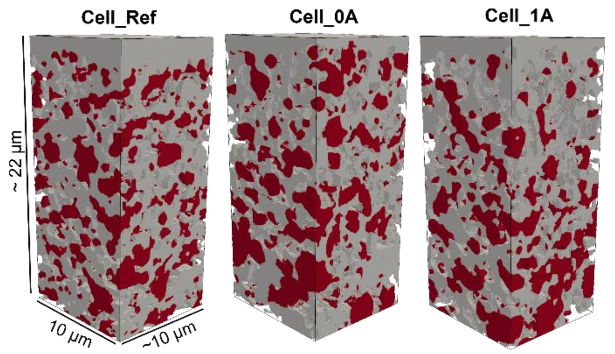

Fig. 4 3D microstructural renderings extracted from the FIB-SEM datasets of Cell_Ref, Cell_0A, and Cell_1A. Ni, YSZ, and pores are colored in red, gray, and transparent, respectively.

Table 1 summarizes the microstructural properties quantified on the active electrode and the support layer of each cell. In the following the parameters of active electrodes are firstly discussed. The Ni phase volume fraction shows a decrease from 28.9% in Cell_Ref to 20.9% in Cell_1A, whereas that of Cell_0A is 27.9%. Taking the experimental uncertainty into account, it can be concluded that the Ni phase volume fraction in the active electrode of Cell_0A remains more or less unchanged in comparison with that of Cell_Ref. Meanwhile, the porosity shows an increase from around 24.3% in Cell_Ref to 26.4% in Cell_0A and further to 36.0% in Cell_1A. The YSZ phase volume fraction exhibits a slight difference, 46.8%, 45.7%, and 44.2% for Cell_Ref, Cell_0A, and Cell_1A, respectively. Since the self-diffusion of YSZ is very slow at 800 °C [35], the variations in the YSZ phase fraction indicate the level of accuracy for 3D reconstruction and the following analysis (including the errors from image post-processing and segmentation together with the volume size limitation) plus the structure inhomogeneity [36, 37]. The total and percolating TPB length show a slight increase in Cell_0A (2.29 μm/μm³ and 1.92 μm/ μm³) and a pronounced decrease in Cell_1A (1.53 μm/μm³ and 0.73 μm/μm³) compared to Cell_Ref (2.29 μm/μm³ and 1.86 μm/μm³). The calculated interface and surface areas are presented in Table 1 as well. Significant reduction of Pore/Ni and YSZ/Ni interface, as well as Ni surface area, can be observed in the comparison of Cell_Ref and Cell_1A, which decrease from 1.39 μm²/μm³, 0.39 μm²/μm³, and 1.00 μm²/μm³ for Cell_Ref to 0.94 μm²/μm³, 0.29 μm²/μm³ and 0.65 μm²/μm³ for Cell_1A, respectively. On the other hand, there is little change in Ni surface area, Pore/Ni interface, and YSZ/Ni interface between Cell_Ref and Cell_0A. The change of Pore/YSZ interface area, Pore surface area, and YSZ surface area among the three cells can be treated as insignificant due to the small variations.

The parameters for the support layer are also discussed. Contrary changes of pore and Ni phase volume fraction can be observed in the support layer compared to the active electrode. Indeed, the phase volume fraction of the pore shows a pronounced reduction from 27. 0% for Cell_Ref to 23.2% for Cell_1A and the Ni phase fraction increases apparently from 28.5% for Cell_Ref to 32.7% for Cell_1A. The variation of pore and Ni phase volume fraction in Cell_0A (30.9% and 26.8%, respectively) compared to Cell_Ref is much minor. The variation of the YSZ phase volume fraction in the support layer is similar to that in the active electrode: 44.4% for Cell_Ref, 42.4% for Cell_0A, and 44.1% for Cell_1A. As already mentioned, this small variation in the YSZ phase volume fraction shall be ascribed to the errors from image post-processing and segmentation together with the inhomogeneity of the sample and the volume size limitation. The variations on the total and percolating TPB length are more pronounced in the support layer for both Cell_0A and Cell_1A compared to Cell_Ref. Therefore, the variations of the TPB length can be attributed to the coarser microstructure of the support layer compared to the active layer (and, to a lesser extent, the uncertainty of the 3D reconstruction method). The microstructure inhomogeneity for the support layer can also be demonstrated by the unexpected fluctuation of YSZ surface area, 2.17 μm²/μm³ for Cell_Ref, 1.74 μm²/μm³ for Cell_0A, and 1.96 μm²/μm³ for Cell_1A obtained from calculation. This also means that the representative volume size is significantly larger for the support layer due to the coarser and inhomogeneous microstructure than that in the active electrode.

Table 1 Microstructural parameters calculated from the reconstructed 3D volumes of the active Ni/YSZ electrode and support layer for Cell_Ref, Cell_0A, and Cell_1A.

	Active Electrode			Support Layer		
	Cell_Ref	Cell_0A	Cell_1A	Cell_Ref	Cell_0A	Cell_1A
Pore Phase fraction (%)	24.3	26.4	36.0	27.0	30.9	23.2
YSZ Phase fraction (%)	46.8	45.7	44.2	44.4	42.3	44.1
Ni Phase fraction (%)	28.9	27.9	19.9	28.5	26.8	32.7
Total TPB (μm/ μm³)	2.23	2.29	1.53	2.27	1.43	1.85
Percolating TPB (μm/ μm³)	1.86	1.92	0.73	1.83	0.87	1.42
Pore/YSZ interface (μm²/ μm³)	1.29	1.43	1.46	1.32	1.27	1.11
Pore/Ni interface (μm²/ μm³)	0.39	0.39	0.29	0.44	0.36	0.35

YSZ/Ni interface (μm^2/ μm^3)	1.00	0.95	0.65	0.85	0.47	0.84
Pore surface area (μm^2/ μm^3)	1.68	1.81	1.75	1.77	1.63	1.47
YSZ surface area (μm^2/ μm^3)	2.29	2.38	2.11	2.17	1.74	1.96
Ni surface area (μm^2/ μm^3)	1.39	1.34	0.94	1.29	0.83	1.19

Fig. 5 shows the continuous particle size distribution (PSD) for Ni, pore, and YSZ phases of the analyzed cells. The PSD variations of three phases in the active electrodes are illustrated in Fig. 5 a-c, while the ones in the support layers are displayed in Fig. 5 d-f. For the Ni phase (Fig. 5a), the peak of the PSD shifts from around 0.8 μm for Cell_Ref and Cell_0A to 1.0 μm for Cell_1A. Besides, the full width at half maximum (FWHM) of PSD for Cell_Ref is smaller than that for Cell_0A and Cell_1A. Fig. 5b shows that Cell_Ref and Cell_0A have similar PSD for the pore phase with a peak position at approximately 0.5 μm. For Cell_1A, the peak is positioned at around 0.7 μm and is much broader than that for Cell_Ref and Cell_0A. The YSZ phase (Fig. 5c) shows similar PSD patterns for all three cells, even if the position of the peak for Cell_0A is slightly shifted compared to Cell_Ref and Cell_1A. With regard to the support layer, pronounced increase of the peak position for Ni phase PSD of Cell_0A and Cell_1A compared to Cell_Ref can be observed in Fig. 5d, from around 0.8 μm for Cell_Ref to 1.6 μm for Cell_0A and 1.2 μm for Cell_1A. Besides, Cell_0A has more large Ni particles with a diameter of 1.8 – 2.8 μm. For the pore phase shown in Fig. 5e, it shows a similar distribution in all three cells with a peak at around 0.7 μm. An unexpected trend for the PSD of YSZ is found for the Cell_0A (Fig. 5f), showing a few large particles with particle diameter over 2 μm.

From the qualitative observation of Fig. 3 d-f and the analysis of Ni PSD in Fig. 5 a and d, it is clear that the Ni coarsening appears in both Cell_0A and Cell_1A and is more pronounced in the support layers than in the active electrodes. The variation of the PSD for the YSZ phase in Fig. 5 c reveals a rather good microstructure homogeneity of the analyzed volume. The PSD peak position of the YSZ phase for active electrodes is almost the same, whereas it shows a large difference in support layers. It means that the active electrodes are more homogeneous, and their structures are finer than that in the support layers. For the PSD of the pore phase, a pronounced variation of active electrode for Cell_1A compared to Cell_Ref is shown in Fig. 5b, whereas Cell_0A is similar to Cell_Ref. Such variation in Cell_1A is caused by Ni migration away from the electrode/electrolyte interface leaving an empty area (as shown in Fig. 3f).

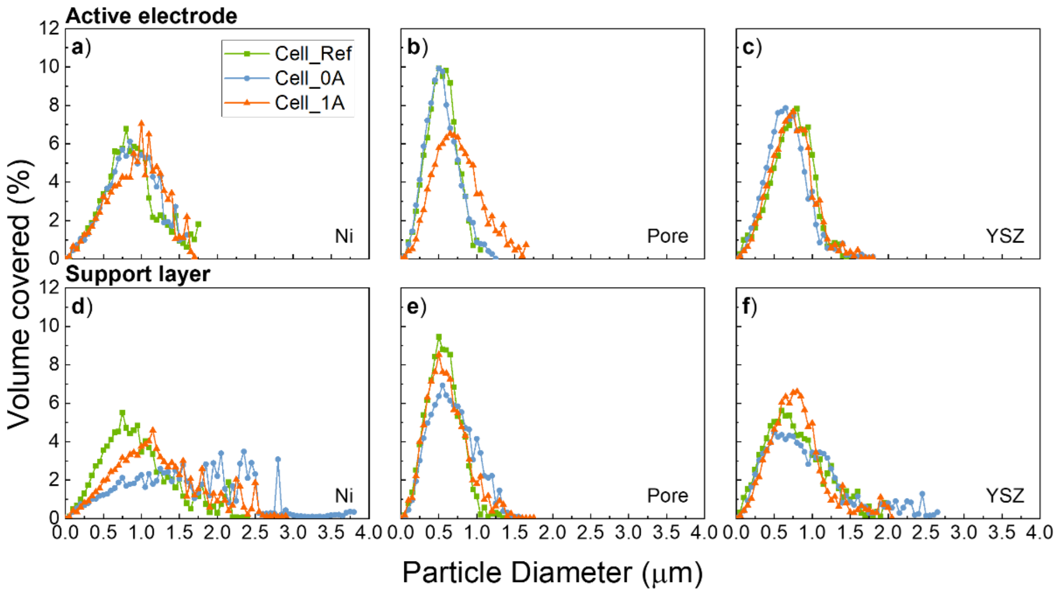

Fig. 5 Continuous particle size distribution (PSD) of the active electrode in Cell_Ref, Cell_0A, and Cell_1A: (a) the Ni PSD, (b) the PSD of pores, and (c) the YSZ PSD; the PSD of support layers in Cell_Ref, Cell_0A, and Cell_1A for (d) Ni phase, (e) pores, and (f) YSZ.

The phase volume fractions of the three cells are illustrated in Fig. 6 and used as further evidence of nickel migration in the electrode. Due to the inhomogeneity of the experimental structure, it is not easy to precisely define the interface between the electrode and the electrolyte. As shown in Fig. 6, the left grey dashed line is placed as the electrolyte/electrode interface, where the YSZ phase fraction drops down sharply and hereafter becomes relatively stable. The 10 µm region between the two dashed grey lines is the active electrode area, and the part right to the second grey dashed line belongs to the support layer. A significant decrease in the Ni phase fraction is observed in the active electrode after the long-term operation at high

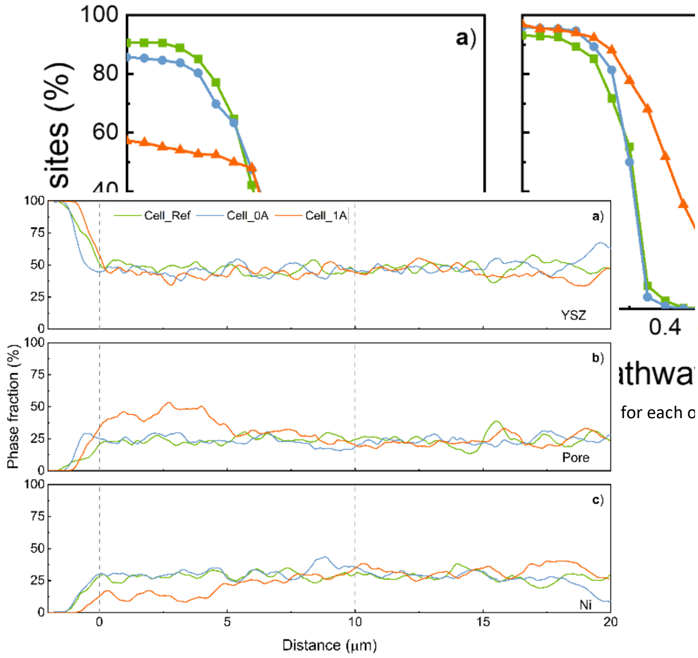

Fig. 6 The phase fraction of the pore, YSZ, and Ni phases versus distance for Cell_Ref, Cell_0A and Cell_1A. The calculation volume of the cells is 10 × 22 × 12.9 µm^3. The grey dashed line at 0 µm represents the electrolyte/electrode interface and the grey dashed line at 10 µm divides the active electrode and the support layer.

current load (i.e., Cell_1A), especially near the electrolyte/electrode interface (from around 0-6 µm), whereas the Ni migration is not apparent in the support layer. The structure is more inhomogeneous in the support layer compared to the active electrode by observing the YSZ volume fraction.

To further quantify the Ni migration in Cell_1A, the position for the volumetric center of the pore, YSZ, and Ni phases in all three cells was calculated in terms of the current direction coordinate starting from the electrolyte toward the support layer. The analyzed volume includes the 10 µm thick active electrode and the 10 µm thick support layer. Fig. 7 shows the variation in the position of the volumetric center for the three phases. Considering that the YSZ phase is stable under the operating conditions, the tiny difference for the YSZ phase among Cell_Ref, Cell_0A and Cell_1A (9.94, 9.94 and 9.92 µm, respectively) can give an impression on the uncertainties caused by the reconstruction, the volume size limitation as well as the structure homogeneity of the cells. Comparing Cell_0A with Cell_Ref, the positions of the volumetric center for all three phases show almost no change. This is however not the case between Cell_1A and Cell_Ref. For the pore phase, the center moved from 10.16 µm in Cell_Ref to 8.70 µm in Cell_1A, whereas the Ni phase shows an opposite trend moving from 10.00 µm in Cell_Ref to 11.64 µm in Cell_1A. Both illustrate that Ni moves away from the electrolyte/electrode interface towards the support layer during the long-term CO_2 electrolysis operation at a high current load (i.e. -1 A/cm^2).

Fig. 7. The position of the volumetric center for the pore, YSZ, and Ni phases in Cell_Ref, Cell_0A, and Cell_1A. The analyzed volume has a dimension of 10 × 20 × 12.9 µm^3, starting from the

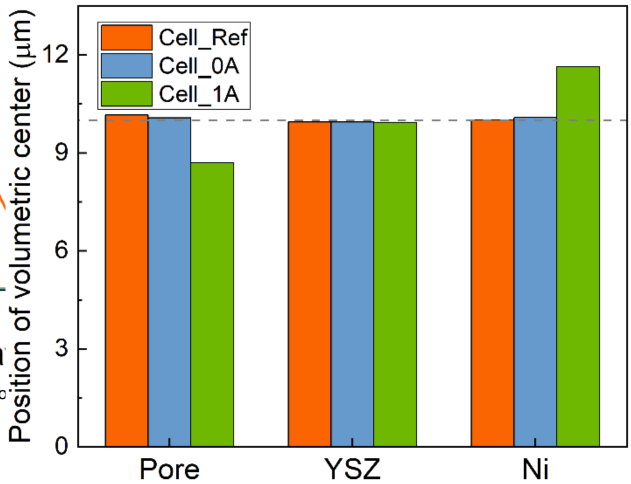

Fig. 7 The position of the volumetric center for the pore, YSZ, and Ni phases in Cell_Ref, Cell_0A, and Cell_1A. The analyzed volume has a dimension of 10 × 20 × 12.9 µm^3, starting from the electrolyte/electrode interface toward the support layer in the current direction (20 µm). The position is expressed in term of the current direction coordinate, with 0 corresponding to the electrolyte/electrode interface, 10 to the electrode/support layer interface (the dashed line in the figure), 20 to the edge of the analyzed volume.

electrolyte/electrode interface toward the support layer in the current direction (20 µm). The position is expressed in term of the current direction coordinate, with 0 corresponding to the electrolyte/electrode interface, 10 to the electrode/support layer interface (the dashed line in the figure), 20 to the edge of the analyzed volume.

The critical pathway diameter, which represents the diameter of the largest sphere that can pass through the phase network, is a parameter to evaluate the quality of the pathway connections of phases (i.e., the pathway widths of the Ni network for the electrons, the pore size for the gas phase and the YSZ phase for oxide ions). This morphological parameter is critical for understanding the quality of the pathways for the three phases in the active electrode, connecting electrochemical properties and microstructure information. If the pathway shows a larger diameter (e.g., 200 nm or above), it is beneficial for the diffusion of gas in the pore phase, ions in the YSZ phase, and electrons in Ni networks. Since the electrochemical reactions take place mainly in the active electrode, the critical pathway diameter is calculated only for this part of the three cells, as shown in Fig. 8. A significant variation of the critical pathway diameter for the Ni phase can be observed in Fig. 8a. The percentage of the pathway with a diameter over 200 nm is around 90% for Cell_Ref, and slightly decreased but still over 80% for Cell_0A. In Cell_1A less than 60% of the TPB sites are percolating through the Ni phase. The characteristic drop-off seems to be at a similar size (around 400 nm) for all the three cells, indicating that deterioration of the Ni phase network is the main cause of the poor TPB percolation. With regard to the pore phase (Fig. 8b), Cell_Ref and Cell_0A behave similarly, but Cell_1A behaves significantly different. The percentage of percolating TPB sites with a pathway diameter over 200 nm is much higher in Cell_1A as compared to Cell_Ref and Cell_0A. For the YSZ phase, all three cells show similar pattern as displayed in Fig. 8c. The results illustrated in Fig. 8 confirm the degradation trends observed in Fig. 3 and Fig. 5. Ni coarsening occurs in both Cell_0A and Cell_1A, resulting in a slight degradation of the critical pathway diameter of the Ni phase. Whereas the Ni migration happening only in Cell_1A is the main cause of the decrease in the Ni critical pathway diameter.

Discussion

In order to clarify the mechanism of Ni migration during long-term electrolysis operation, we compared our results presented in this work to the findings published previously by Trini et al. from the same group, but on cells tested for steam electrolysis [8]. Similar types of cells were used in these studies, thus allowing us to make quantitative comparisons on cell degradation and associated microstructural changes. Ni/YSZ supported SOEC cells with the same cell configuration but from different production batches were used in these studies. In Trini's work one cell was tested at 800 °C and -1 A/cm^2 for steam electrolysis over 1000 h and the result of this cell is then compared with those of Cell_1A from the current work, as presented in Table 2. Both cells were tested at 800 °C and -1 A/cm^2 (with 56% steam or CO_2 conversion) for 1000 h and show similar degradation rates: 8.2 %/kh for Cell_1A tested for CO_2 electrolysis and 8.3 %/kh for the one in Ref 8 tested for steam electrolysis. The two types of cells differ slightly in the initial Ni/YSZ electrode microstructure, as reflected in total and percolating TPBs at 0 h presented in Table 2. The difference could be caused by small variations in cell production, cell reduction and 3D reconstruction. After around 1000 h testing, the cell tested in CO_2 electrolysis shows a bit more pronounced loss in total and percolating TPBs than the one in steam electrolysis.

However, the microstructural evolution of the active Ni/YSZ electrode is not exactly the same between the two cells, especially on the extent of Ni migration and the loss of the percolating TPBs, as presented in Table 2. The two cells exhibit similar characteristics in initial Ni/YSZ microstructure, e.g. 2.23 and 1.86 µm/µm^3 for Cell_Ref (this work), and 2.44 and 2.19 µm/µm^3 for Cell_Ref_Steam, for total and percolating TPBs respectively. After around 1000 h electrolysis testing, the cell tested in CO_2 electrolysis (Cell_1A) shows a more pronounced deterioration in the active Ni/YSZ electrode than the one tested in steam electrolysis (Cell_1A_Steam): a 60.75% loss in percolating TPBs and a 8 µm thick Ni migration zone for the cell tested in CO_2 electrolysis as compared to a 37.90% loss in percolating TPBs and a 4 µm thick Ni migration zone for the cell tested in steam electrolysis. Table 2 also presents the measured cell electrochemical performance. It can be noted that the increase in the R_s is higher for the cell operated in CO_2 electrolysis than the one in steam electrolysis. This correlates well with the fact that the extent of Ni migration is more significant in CO_2 electrolysis than in steam electrolysis.

The Ni coarsening and depletion at the electrode/electrolyte interface observed in this study is consistent with the results reported in Ref [22] for a standard cell tested under CO_2 electrolysis. Therefore, it can be claimed that Ni migration away from the electrolyte interface also take place under CO_2 electrolysis. This microstructural evolution cannot be fully explained by the hypotheses reported in literature. Mogensen et al. [18] proposed a hypothesis that in the H_2O/H_2 atmosphere, Ni migrates in the form of $Ni(OH)_x$ species via surface diffusion below 800 °C and gas diffusion above 900 °C. However, $Ni(OH)_x$ species do not exist in dry CO_2/CO atmospheres. Therefore, $Ni(OH)_2$ diffusion alone is not able to explain the Ni migration in CO_2 electrolysis. Another hypothesis claims that the contact angle gradient (interface energy gradient) is the driving force of Ni migration [8, 20]. In this work, the mechanism of Ni coarsening and migration is further discussed. Generally speaking, there are two kinds of driving forces causing the Ni rearrangement during the long-term electrolysis operation: 1) the gradient in the partial pressure of Ni-containing gas species [7, 18], which claims that the Ni may migrate down the local pO_2 (pH_2O/pH_2) gradient in the form of $Ni(OH)_x$, and 2) the minimization of the interfacial energy [38], which is related to the contact angle of Ni and YSZ phases. The partial pressure driven mechanism is strongly influenced by the partial pressure of Ni-containing gas species. Fig. 9 shows the total and partial pressure of Ni gas species over the solid flat Ni at 800 °C as a function of the CO_2 or steam fraction from 0 to 0.99 calculated using FACTSAGE software and databases [39]. The Ni phase is stable without oxidation in the CO_2 or steam fraction range from 0 to 0.99. The top x-axis plots the corresponding oxygen partial pressure, which increases as the increase of CO_2 or H_2O. There are three Ni-containing gas species (i.e. $Ni(CO)_4$, Ni, and NiO) in CO_2/CO atmosphere and four Ni-containing gas species (i.e. $Ni(OH)_2$, NiH, Ni, and NiO) in H_2O/H_2 atmosphere. It can be observed that in the atmosphere of CO_2/CO (90/10), the total partial pressure of Ni gas species is 7.06×10^{-14} atm, while in the atmosphere of H_2O/H_2 (50/50), the total partial pressure of Ni gas species is 2.67×10^{-11} atm. The total partial pressure of Ni gas species remains almost constant when the $pCO_2 > 0.5$ atm (SOEC mode), while in the H_2O/H_2 atmosphere, the total partial pressure of Ni gas species increases apparently from around 10^{-11} to 10^{-8} atm when pH_2O increases from 0.5 to 0.99 atm.

It is difficult to experimentally evaluate the contribution of the gas diffusion pathway on Ni rearrangement. Lei et al. [40] conducted phase-field simulations and concluded that pH_2O affects the Ni coarsening only at $pH_2O > 0.9$ atm, i.e. when the partial pressure of Ni gas species is higher than 10^{-10} atm. In addition, a gradient in the partial pressure of Ni gas species is required in order to drive Ni to diffuse from high to low partial pressure. As shown in Fig. 9a, in CO_2 electrolysis at 800 °C, the partial pressure of Ni-containing gas species is around 10^{-13} atm irrespective of the $pCO_2/(pCO+pCO_2)$ composition, indicating that the gas phase diffusion pathway may have insignificant contribution to both Ni coarsening and Ni migration in CO_2/CO atmosphere. Mihaylov et al.[41] investigated the formation of $Ni(CO)_4$ during interaction of CO with silica-supported highly dispersed nickel metal utilizing FTIR (Fourier transform infrared) spectroscopy. In combination with previous studies [42, 43], they reported that $Ni(CO)_4$ prefers to form with large CO quantity at 350-390 K, and the formation rate drops sharply with increasing temperature. This indicates that the Ni gas species $Ni(CO)_4$ may hardly form under the high temperature electrolysis condition, which is consistent with the calculation results in Fig.9a.

With regard to the surface/interface energy minimization mechanism, the gradient in the Ni-YSZ contact angle (i.e. wettability gradient) was proposed as the driving force for Ni migration. Jiao et al.[44] proposed that the variation of the Ni-YSZ contact angle is caused by the gradient of pO_2 associated with the local over-potential of the fuel electrode. However, Trini et al. pointed out that such gradient is not enough to drive the Ni migration observed experimentally [8]. Besides, the effect of the polarization on the work of adhesion at the Ni-YSZ interface, which can cause a larger contact angle gradient, is also studied [20]. However, the quantitative correlation between polarization overpotentials and work of adhesion still needs to be discussed. Monaco et al. [16] proposed that the work of adhesion between Ni and YSZ could be affected by the electrode over-potential through the accumulation of oxygen vacancies in the electrochemical double layer at the Ni-YSZ interface, which also affects the contact angle between Ni and YSZ. In the following, we calculate the Ni-YSZ contact angle through the electrode thickness along the current direction using models developed by Jiao et al. [20, 44] and Monaco et al. [16, 45]. In order to assess the gradient of contact angles through the electrode thickness, the fuel electrode overpotential at the electrolyte interface ($\eta_{\text{fuel}}(x=0)$) has been estimated with the corresponding electrode resistance values listed in Table 2 [32, 46]. Then, the local oxygen partial pressure at the electrolyte interface (i.e. for x=0: cf. Fig. 10) can be assessed according to the Nernst equation [13].

$$\eta(x) = \frac{RT}{4F}\ln\left(\frac{p_{\text{local}}O_2(x)}{p_{\text{gas}}O_2}\right) \tag{1}$$

Table 2 Electrochemical and microstructural degradation of the Ni/YSZ electrodes in the cells operated at 800 °C and -1 A/cm² for CO_2 or steam electrolysis.

	CO_2/CO (90/10)		H_2O/ H_2 (50/50) [8]	
Electrochemical performance	Cell_1A		Cell_1A_Steam	
	0h	1083h	0h	1000h
V_{cell} (mV)	1199.73	1298.73	1246.00	1349.42
$E°$ (mV)	880.04	880.04	977.31	977.31
R_s (Ω cm²)	0.105	0.123	0.076	0.076
R_{ion} (Ω cm²)	0.022	0.038	0.033	0.052
$R_{\text{Ni/YSZ\_TPB}}$ (Ω cm²)	0.099	0.192	0.114	0.210
$R_{\text{diff}} + R_{\text{conv}}$	0.041	0.054	0.150	0.176
η_{fuel} (mV)	-97.66	-167.14	-89.07	-166.48
Microstructure parameters	Cell_Ref	Cell_1A	Cell_Ref_Steam	Cell_1A_Steam
Total TPBs (µm/ µm³)	2.23	1.53	2.44	1.47
Percolating TPBs (µm/ µm³)	1.86	0.73	2.19	1.36
Ni migration zone	around 8 µm		around 4 µm	

where R is the ideal gas constant (8.314 J/K/mol), and F is the Faraday constant equal to 96485 C/mol. The term $p_{\text{gas}}O_2$ is the equilibrium oxygen partial pressure for the inlet gas. It can be calculated according to the equilibrium of H_2O, H_2, and O_2 for steam electrolysis, and that of CO_2, CO, and O_2 for CO_2 electrolysis:

$$pO_2 = \frac{1}{K_H}\left(\frac{pH_2O}{1-pH_2O}\right)^2 \text{ or } pO_2 = \frac{1}{K_H}\left(\frac{pCO_2}{1-pCO_2}\right)^2 \tag{2}$$

where K_H is the equilibrium constant, and it equals to 2.29×10^{18} for H_2O/H_2 reaction, and 2.76×10^{18} for CO_2/CO reaction at 800 °C [39]. $p_{\text{local}}O_2(x)$ represents the oxygen partial pressure at the active TPBs. $p_{\text{local}}O_2(x)/p_{\text{gas}}O_2$ is proportional to the activity of the surface adsorbed oxygen (a_O), which is related to the Ni surface tension causing the variation of contact angle. The detailed description can be found in Ref [44]. In this work, for simplicity, we take the thickness of the active Ni/YSZ electrode as 10 µm. Therefore, at the other end of the active layer (x=10 µm), i.e. at the interface between the active electrode and the support layer, the local electrode overpotential drops to zero and the local oxygen partial pressure is equal to the one of the inlet gas: $p_{\text{local}}O_2(x=10\ \mu m) = p_{\text{gas}}O_2$. Between these two bounds, $p_{\text{local}}O_2(x=0\ \mu m)$ and $p_{\text{local}}O_2(x=10\ \mu m)$, a linear change in $p_{\text{local}}O_2$ is assumed. According to Jiao's model, the contact angle of Ni/YSZ across the active layer $\theta_{Ni/YSZ}(x)$ can be deduced from the evolution of local oxygen partial pressure $p_{\text{local}}O_2(x)$ [44]:

$$\theta_{\frac{Ni}{YSZ}}(x) = \cos^{-1}\left(\frac{W_{\text{ad}}}{\gamma^p - \Gamma_O RT\ln\left(1+K_a\left(2.38\times10^{-4}\left(\frac{p_{\text{local}}O_2(x)}{p_{\text{Total}}}\right)^{0.5}\exp\left(\frac{1.82\times10^5}{RT}\right)\right)\right)} - 1\right) \tag{3}$$

where W_{ad} is the work of adhesion at the Ni/YSZ interface, and a constant value of 1.4 J/m^2 is assumed in this work [47], γ^p is the surface tension of pure Ni without oxygen adsorption and equals to 1829 - 0.4014 × (T - 1728) (10^{-3} N/m), Γ_O is the saturation coverage of oxygen adsorption on Ni surface which equals to 0.481 N/m [48], and K_a is the oxygen adsorption coefficient approximated to be 1200 [49]. The term p_{Total} denotes the atmospheric pressure. The contact angle $\theta_{Ni/YSZ}$ is plotted

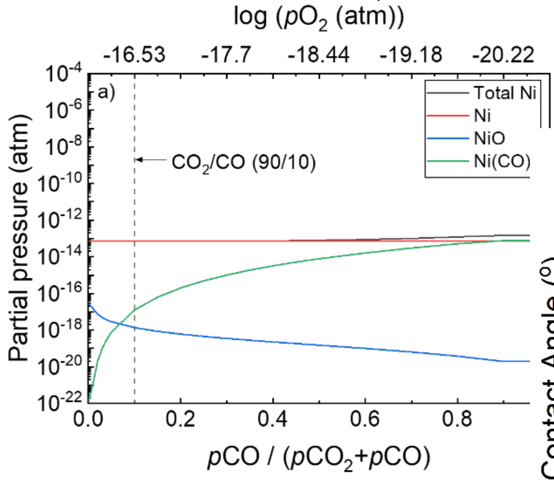

Fig. 9 Calculated partial pressure of Ni gas species over sol atmosphere.

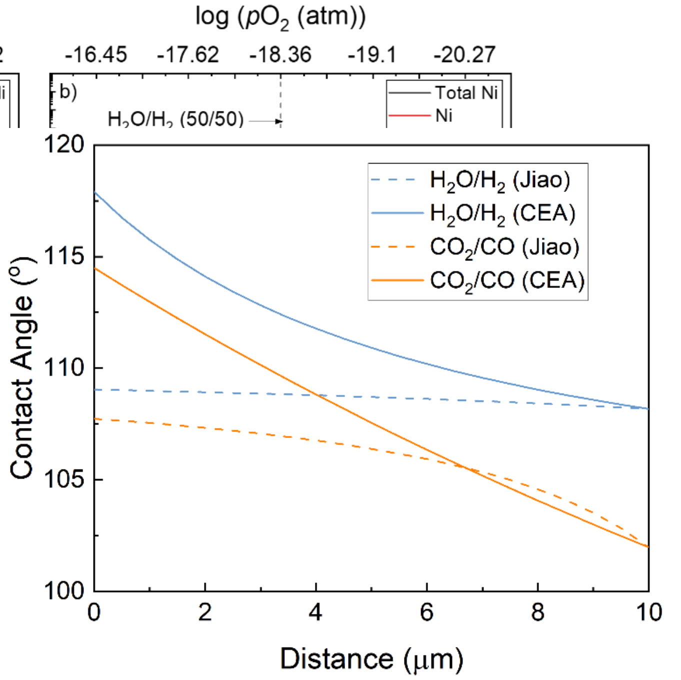

Fig. 10 Relation between the contact angle and distance x to the electrode/electrolyte interface (x=0) for H_2O/H_2 (50/50) (blue lines) and CO_2/CO (90/10) (orange lines) electrolysis. Dashed lines represent the contact angle calculated according to Jiao's work [44], and solid lines represent the contact angle calculated according to Monaco and Rorato's model (CEA) [45].

as function of position x in the active layer in Fig. 10 (the blue and orange dashed lines for steam and CO_2 electrolysis, respectively). For both steam and CO_2 electrolysis, the Ni-YSZ contact angle decreases along the current direction from the electrolyte/electrode interface to the electrode/support interface, but the gradient is rather small. Among which, the gradient in CO_2 electrolysis is slightly higher than the one in steam electrolysis. Such small gradients cannot account for the experimentally observed Ni migration in SOEC mode, as pointed out also by Trini et al. [8].

Monaco et al. and Rorato et al. [16, 45] claim that besides pO_2, the over-potential also affects the accumulation of oxygen vacancies in the electrochemical double layer, which influences the contact angle of Ni and YSZ. Considering a blocking electrode (i.e. in the middle of the Ni/YSZ interface away from the TPBs lines), the concentration of vacancies in the vicinity of the Ni/YSZ interface can be estimated as a function of the distance in the electrode through the local over-potential $\eta(x)$ [50]:

$$C_{V_{\ddot{O}}}(x) = \frac{C_{V_{\ddot{O}}}^{max} C_{V_{\ddot{O}}}^{8YSZ} \exp(-\frac{2F}{RT}\eta(x))}{C_{V_{\ddot{O}}}^{max} + C_{V_{\ddot{O}}}^{8YSZ}\left(\exp\left(-\frac{2F}{RT}\eta(x)\right) - 1\right)} \quad (4)$$

$C_{V_{\ddot{O}}}(x)$ denotes the oxygen vacancy concentration at the Ni/YSZ interface, and $C_{V_{\ddot{O}}}^{max}$ and $C_{V_{\ddot{O}}}^{8YSZ}$ are the maximum and the bulk concentrations in YSZ, equal to 98113.3 and 3924.5 mol/m^3, respectively. According to the Eq (1), $\eta(x)$ can be calculated assuming a linear relationship between gas composition and distance. Therefore, the concentration of vacancies in the double layer can be estimated through the electrode thickness with Eq (4). To relate this concentration to the contact angles, a linear dependence has been assumed between the two quantities. To establish this relation, it is worth mentioning that $C_{V_{\ddot{O}}}(x = 10\ \mu\mathrm{m})$ is equal to the concentration in the bulk $C_{V_{\ddot{O}}}^{8YSZ}$, and hence, the corresponding contact angle $C_{V_{\ddot{O}}}(x = 10\ \mu\mathrm{m})$ can be expressed by Eq (3). Besides, it has been assumed that the Ni particles detach from YSZ (i.e. $\theta_{Ni/YSZ}^{max} = 180°$) when the concentration of vacancies reaches $C_{V_{\ddot{O}}}^{max}$. Thanks to this linear dependence, the contact angle $\theta_{Ni/YSZ}^{\eta}(x)$ can be calculated as a function of the position in the electrode thickness as shown in Fig. 10 (where the blue and orange solid lines are referred to steam and CO_2 electrolysis, respectively). It can be noticed that $\theta_{Ni/YSZ}^{\eta}(x = 0)$ at the electrode/electrolyte interface calculated using Monaco and Rorato's model is roughly 10° larger than $\theta_{Ni/YSZ}(x = 0)$ calculated using Jiao's model.

Also, Monaco and Rorato's model predicts larger gradients in the contact angle for both steam and CO_2 electrolysis. Starting from the electrolyte/electrode interface, both curves have similar slope from 0 to around 4 μm. Hereafter, the curve for steam electrolysis starts to flatten out, while the one for CO_2 keeps the same slope. The contact angle curves predicted using Monaco and Rorato's model seems to fit better with the observed Ni migration as summarized in Table 2, than the one using Jiao's model, thus can qualitatively explain the Ni migration for steam and CO_2 electrolysis. Using the same model and combined with phase field modelling simulations, Rorato et al. [51] reproduced the different Ni migration phenomena in SOFC and SOEC modes. According to their results, a pronounced Ni migration away from the electrolyte is predicted in SOEC mode, which is consistent with our experimental results. In SOFC mode, a small extent of Ni migration towards the electrolyte is anticipated. Such a small movement of Ni may not be observed experimentally due to errors from 3D reconstruction and inhomogeneity of Ni-YSZ electrode local microstructure. Most experimental results show that Ni coarsening is the main degradation of Ni/YSZ electrode in SOFC mode [8, 52, 53]. However, Menzler et al. [54] conducted post-test characterization on an SOFC stack tested at 700 °C and 0.5 A cm^{-2} for 100,000 h, and observed Ni enrichment in the Ni/YSZ electrode near the electrolyte. This is consistent with our phase field simulations [51]. These findings seem to indicate that Ni migrates towards the electrolyte in SOFC mode, but the extent of Ni migration is much less than in SOEC mode in the opposite direction (i.e. towards the support layer). Further quantification of microstructure evolution in long-term tested Ni-YSZ electrodes in SOFC mode is needed to clarify the mechanism.

Conclusions

In this work, detailed 3D microstructural characterizations of the Ni/YSZ electrode after long-term operation in CO_2 electrolysis were conducted. Three cells were selected for the study, Cell_Ref where the cell experienced reduction only, Cell_0A, and Cell_1A where the cells were operated at 0 or -1 A/cm^2 for 1000 h at 800 °C, respectively. The coarsening of Ni can be observed both in the support layer and active layer of Cell_0A and Cell_1A. The same type of analysis performed on the YSZ backbone confirms the stability of this ceramic phase during the operation. The migration of Ni in the region close to the electrode/electrolyte interface toward the support layer can only be observed in Cell_1A, indicating that current plays a major role for Ni migration. By analyzing the 3D Ni/YSZ electrode microstructures, a significant loss of Ni in the active electrode is observed in Cell_1A, along with an increased Ni phase fraction in the support layer. An increase of the Ni particle size (i.e. Ni coarsening) is also observed. Whereas in Cell_0A, only Ni coarsening is observed, but without Ni migration. Our results show that Ni migration away from the electrolyte/electrode interface happens also during long-term CO_2 electrolysis. Different possible mechanisms accounting for the Ni depletion under CO_2 electrolysis have been discussed. It seems that the contribution from the gas diffusion pathway is minor under the conditions explored in this work. The gradient in the Ni-YSZ contact angle may play a significant role, driving the Ni surface diffusion in both CO_2 and steam electrolysis.

CRediT authorship contribution statement

Yijing Shang: Investigation, Data curation, Visualization, Writing - original draft; Anne Lyck Smitshuysen, Yuliang Liu, Miao Yu and Xiaofeng Tong: Investigation; Peter Stanley Jørgensen: Supervision, Writing – review & editing; Léa Rorato and Jérôme Laurencin: Writing – review & editing; Ming Chen: Conceptualization, Funding acquisition, Resources, Data curation, Investigation, Supervision, Writing – review & editing.

Conflicts of interest

The authors declare no conflicts of interest.

Acknowledgment

This work was supported by the project "Efficient Power2Gas Combining SOEC and Biomass Gasification" (EUDP no. 64017-0011). Yijing Shang acknowledges financial support from the China Scholarship Council (CSC202006370036) and from DTU Energy. Xiaofeng Tong acknowledges support from the National Natural Science Foundation of China (Grant no. 52102244). The projects "Integrated Energy Conversion and Control for Smart and Efficient Electrolysis Systems (IECC)" (IFD project no. 8087-00019B) and "Next Generation Power2X for Renewable Energy Conversion and Storage (NEXP2X)" (IFD no. 0143-00009B) are further acknowledged for support in finalizing the manuscript.

Reference

1. B. Rego de Vasconcelos and J. M. Lavoie, *Front. Chem.*, 2019, **7**, 392.
2. C. Graves, S. D. Ebbesen, M. Mogensen and K. S. Lackner, *Renewable Sustainable Energy Rev.*, 2011, **15**, 1-23.
3. S. D. Ebbesen, S. H. Jensen, A. Hauch and M. B. Mogensen, *Chem. Rev.*, 2014, **114**, 10697-10734.
4. D. The, S. Grieshammer, M. Schroeder, M. Martin, M. Al Daroukh, F. Tietz, J. Schefold and A. Brisse, *J. Power Sources*, 2015, **275**, 901-911.
5. Q. Fang, C. E. Frey, N. H. Menzler and L. Blum, *J. Electrochem. Soc.*, 2018, **165**, F38-F45.
6. M. P. Hoerlein, M. Riegraf, R. Costa, G. Schiller and K. A. Friedrich, *Electrochim. Acta*, 2018, **276**, 162-175.
7. M. B. Mogensen, A. Hauch, X. Sun, M. Chen, Y. Tao, S. D. Ebbesen, K. V. Hansen and P. V. Hendriksen, *Fuel Cells*, 2017, **17**, 434-441.
8. M. Trini, A. Hauch, S. De Angelis, X. Tong, P. V. Hendriksen and M. Chen, *J. Power Sources*, 2020, **450**, 227599.
9. H. Moussaoui, A. Nakajo, G. Rinaldi, M. Hubert, J. Laurencin and J. V. herlea, *ECS Trans.*, 2021, **103** 997-1009
10. X. Sun, Y. Liu, P. V. Hendriksen and M. Chen, *J. Power Sources*, 2021, **506**, 230136.
11. A. Hauch, S. D. Ebbesen, S. H. Jensen and M. Mogensen, *J. Electrochem. Soc.*, 2008, **155**, B1184.
12. Y. Tao, S. D. Ebbesen and M. B. Mogensen, *J. Power Sources*, 2016, **328**, 452-462.
13. M. Chen, Y.-L. Liu, J. J. Bentzen, W. Zhang, X. Sun, A. Hauch, Y. Tao, J. R. Bowen and P. V. Hendriksen, *J. Electrochem. Soc.*, 2013, **160**, F883-F891.
14. Y. Yan, Q. Fang, L. Blum and W. Lehnert, *Electrochim. Acta*, 2017, **258**, 1254-1261.

15. N. H. Menzler, D. Sebold and S. Zischke, *ECS Trans.*, 2019, **91**, 719-729.
16. F. Monaco, M. Hubert, J. Vulliet, J. P. Ouweltjes, D. Montinaro, P. Cloetens, P. Piccardo, F. Lefebvre-Joud and J. Laurencin, *J. Electrochem. Soc.*, 2019, **166**, F1229-F1242.
17. X. Sun, P. V. Hendriksen, M. B. Mogensen and M. Chen, *Fuel Cells*, 2019, **19**, 740-747.
18. M. B. Mogensen, M. Chen, H. L. Frandsen, C. Graves, A. Hauch, P. V. Hendriksen, T. Jacobsen, S. H. Jensen, T. L. Skafte and X. Sun, *Fuel Cells*, 2021, DOI: 10.1002/fuce.202100072, 415-429.
19. Z. Jiao, N. Shikazono and N. Kasagi, *J. Electrochem. Soc.*, 2012, **159**, B285-B291.
20. Z. Jiao, E. P. Busso and N. Shikazono, *J. Electrochem. Soc.*, 2020, **167**, 024516.
21. T. L. Skafte, Z. Guan, M. L. Machala, C. B. Gopal, M. Monti, L. Martinez, E. Stamate, S. Sanna, J. A. Garrido Torres, E. J. Crumlin, M. García-Melchor, M. Bajdich, W. C. Chueh and C. Graves, *Nature Energy*, 2019, **4**, 846-855.
22. A. Hauch, M. L. Traulsen, R. Küngas and T. L. Skafte, *J. Power Sources*, 2021, **506**, 230108.
23. A. Sciazko, Y. Komatsu, A. Nakamura, Z. Ouyang, T. Hara and N. Shikazono, *Chem. Eng. J.*, 2023, **460**.
24. C. Graves, *Journal*, 2012.
25. P. S. Jørgensen, S. L. Ebbehøj and A. Hauch, *J. Power Sources*, 2015, **279**, 686-693.
26. B. Münch and L. Holzer, *J. Am. Ceram. Soc.*, 2008, **91**, 4059-4067.
27. P. S. Jørgensen, K. V. Hansen, R. Larsen and J. R. Bowen, *J. Power Sources*, 2010, **195**, 8168-8176.
28. H. Schichlein, A. C. Müller, M. Voigts, A. Krügel and E. Ivers-Tiffée, *J. Appl. Electrochem.*, 2002, **32**, 875-882.
29. A. Leonide, V. Sonn, A. Weber and E. Ivers-Tiffée, *J. Electrochem. Soc.*, 2008, **155**, B36.
30. V. Sonn, A. Leonide and E. Ivers-Tiffée, *J. Electrochem. Soc.*, 2008, **155**, B675.
31. X. Tong, P. V. Hendriksen, A. Hauch, X. Sun and M. Chen, *J. Electrochem. Soc.*, 2020, **167**, 024519.
32. Y. Yang, X. Tong, A. Hauch, X. Sun, Z. Yang, S. Peng and M. Chen, *Chem. Eng. J.*, 2021, **417**, 129260.
33. S. Ovtar, X. Tong, J. J. Bentzen, K. T. S. Thyden, S. B. Simonsen and M. Chen, *Nanoscale*, 2019, **11**, 4394-4406.
34. M. Chen, X. Sun, C. Chatzichristodoulou, S. Koch, P. V. Hendriksen and M. B. Mogensen, *ECS Trans.*, 2017, **78**, 3077.
35. M. Kilo, M. A. Taylor, C. Argirusis, G. Borchardt, R. A. Jackson, O. Schulz, M. Martin and M. Weller, *Solid State Ionics*, 2004, **175**, 823-827.
36. P. S. Jørgensen, K. Yakal-Kremski, J. Wilson, J. R. Bowen and S. Barnett, *J. Power Sources*, 2014, **261**, 198-205.
37. W. M. Harris and W. K. S. Chiu, *J. Power Sources*, 2015, **282**, 552-561.
38. Z. Jiao and N. Shikazono, *J. Electrochem. Soc.*, 2018, **165**, F55-F63.
39. C. W. Bale, E. Bélisle, P. Chartrand, S. A. Decterov, G. Eriksson, A. E. Gheribi, K. Hack, I. H. Jung, Y. B. Kang, J. Melançon, A. D. Pelton, S. Petersen, C. Robelin, J. Sangster, P. Spencer and M. A. Van Ende, *Calphad*, 2016, **55**, 1-19.
40. Y. Lei, T.-L. Cheng, H. Abernathy, W. Epting, T. Kalapos, G. Hackett and Y. Wen, *J. Power Sources*, 2021, **482**, 228971.
41. M. Mihaylov, K. Hadjiivanov and H. Knözinger, *Catalysis Letters*, 2001, **76**, 59-63.
42. G. Greiner and D. Menzel, *Journal of Catalysis*, 1982, **77**, 382-396.
43. W. M. Shen, J. A. Dumesic and C. G. Hill, *Journal of Catalysis*, 1981, **68**, 152-165.
44. Z. Jiao and N. Shikazono, *Acta Mater.*, 2017, **135**, 124-131.
45. L. Rorato, Y. Shang, S. Yang, M. Hubert, K. Couturier, L. Zhang, J. Vulliet, M. Chen and J. Laurencin, unpublished work.
46. S. C. Singhal, in *Solid Oxide Fuels Cells: Facts and Figures: Past Present and Future Perspectives for SOFC Technologies*, eds. J. T. S. Irvine and P. Connor, Springer London, London, 2013, DOI: 10.1007/978-1-4471-4456-4_1, pp. 1-23.
47. A. Tsoga, A. Naoumidis and P. Nikolopoulos, *Acta Mater.*, 1996, **44**, 3679-3692.
48. S. Ozawa, S. Takahashi, N. Watanabe and H. Fukuyama, *Int. J. Thermophys.*, 2014, **35**, 1705-1711.
49. G. R. Belton, *Metall. Mater. Trans. B*, 1976, **7**, 35-42.
50. M. G. H. M. Hendriks, J. E. ten Elshof, H. J. M. Bouwmeester and H. Verweij, *Solid State Ionics*, 2002, **146**, 211-217.
51. L. Rorato, Y. Shang, S. Yang, M. Hubert, K. Couturier, L. Zhang, J. Vulliet, M. Chen and J. Laurencin, *J. Electrochem. Soc.*, 2023.
52. Z. Jiao, T. Shimura and N. Shikazono, *ECS Trans.*, 2015, **68**, 1281-1289.
53. M. Hubert, J. Laurencin, P. Cloetens, B. Morel, D. Montinaro and F. Lefebvre-Joud, *J. Power Sources*, 2018, **397**, 240-251.
54. N. H. Menzler, D. Sebold, Y. J. Sohn and S. Zischke, *J. Power Sources*, 2020, **478**.